

# Full-scale investigation of heliostat aerodynamics through wind and pressure measurements at a pentagonal heliostat

Kristina Blume<sup>a,\*</sup>, Marc Röger<sup>b</sup>, Robert Pitz-Paal<sup>c</sup>

<sup>a</sup> German Aerospace Center (DLR), Institute of Solar Research, Karl-Heinz-Beckurts Str. 13, 52428 Jülich, Germany

<sup>b</sup> German Aerospace Center (DLR), Institute of Solar Research, Paseo de Almería 73, 04001 Almería, Spain

<sup>c</sup> German Aerospace Center (DLR), Institute of Solar Research, RWTH Aachen University, Chair of Solar Technology, Linder Höhe, 51147 Cologne, Germany

## ARTICLE INFO

### Keywords:

Solar tracker  
Heliostat  
Wind load  
Full-scale investigation  
Pressure distribution  
Aerodynamic admittance

## ABSTRACT

Wind loads on heliostats are often investigated through experimental wind tunnel studies or numerical simulations. However, these approaches cannot consider the full-scale conditions but require a reproduction and simulation of both the heliostat structure and the wind conditions. Complementary full-scale investigations are therefore crucial but are at the same time relatively costly, as it is cumbersome to set up large heliostats with measurement devices. This paper introduces a new pressure measurement system which is easy-to-apply to a real-scale heliostat and enables full-scale investigations with minimized effort. The results of a first field study are presented during which wind and pressure measurements were taken simultaneously over periods of 10 min at a 48.5 m<sup>2</sup> pentagonal Stello heliostat. The non-dimensional pressure distributions are investigated and it is shown that the mean  $c_p$ -values are very consistent amongst the measurement periods and reach values between 2.2 and 2.6. These values, in turn, are found to agree well with results of a wind tunnel study. Moreover, the behavior of the load coefficients with varying angles of attack is studied and the aerodynamic admittance functions are evaluated which give in-depth insight into the generation of aerodynamic loads. The admittance functions are found to start decreasing at a non-dimensional frequency of approximately 0.2. This finding indicates that eddies which are about the size of the heliostat or larger are fully effective in generating aerodynamic loads while the effectiveness of smaller eddies is reduced.

## 1. Introduction

Heliostats in a solar tower plant are exposed to turbulent wind within the atmospheric boundary layer and must withstand induced aerodynamic loads regarding survivability and optical performance. To optimize the design of a heliostat, it is therefore crucial to understand the generation of wind loads and their impact on the heliostat. In the past, many wind tunnel studies have been conducted to experimentally investigate wind loads on small-scale heliostats under simulated boundary layer conditions. The determined wind loads of wind tunnel studies are typically generalized by means of non-dimensional mean and peak wind load coefficients which can then be easily transferred into wind loads of real-scale heliostats. Wind tunnel studies are advantageous over full-scale field studies in particular in terms of parameter variation. Parameters that are expected to impact wind loads on heliostats, such as the angle of attack, can be varied and investigated in a relatively easy way. Based on wind tunnel studies, a number of parameters could be identified in the past that lead to variations of heliostat wind load coefficients. Peterka et al. (1989) was amongst

the first to determine wind load coefficients for a variety of different heliostat elevation angles (angle  $\bar{\alpha}$  between the horizontal plane and the concentrator plane, see also Fig. 1) and wind angles of attack (angle  $\bar{\beta}$  between the axis horizontally pointing away from the concentrator and the mean wind direction, see Fig. 1). Furthermore, Peterka et al. (1989) pointed out that the turbulence intensity on elevation axis height was found to significantly affect the coefficients. The impact of the turbulence intensity was further investigated e.g. by Pfahl et al. (2015), Emes et al. (2017) and Yu et al. (2019) who could verify the impact especially on the peak coefficients of heliostats in stow and operational positions. Pfahl et al. (2011b) furthermore investigated the concentrator aspect ratio, reflecting the concentrator shape, and found that wind load coefficients can vary significantly with the aspect ratio. Besides the aspect ratio, the effect of the gap size between the facets was investigated by Wu et al. (2010) and by Pfahl et al. (2011a). While Wu et al. (2010) found that small gaps have a negligible effect on wind load coefficients, Pfahl et al. (2011a) showed that wider gaps can have a significant impact. Moreover, the turbulent integral length

\* Corresponding author.

E-mail address: [kristina.blume@dlr.de](mailto:kristina.blume@dlr.de) (K. Blume).

<https://doi.org/10.1016/j.solener.2022.12.016>

Received 1 August 2022; Received in revised form 1 November 2022; Accepted 11 December 2022

0038-092X/© 2023 The Author(s). Published by Elsevier Ltd on behalf of International Solar Energy Society. This is an open access article under the CC BY license (<http://creativecommons.org/licenses/by/4.0/>).

**Nomenclature**

$A$	Total concentrator area ( $\text{m}^2$ )
$A_n$	Concentrator sub-surface corresponding to triangle $n$ ( $\text{m}^2$ )
$c_L$	Non-dimensional coefficient of load component $L$ (–)
$c_{F_x}$	Drag force coefficient (–)
$c_{F_z}$	Lift force coefficient (–)
$c_{M_{x_h}}$	Moment coefficient about $x_h$ -axis (–)
$c_{M_{y_h}}$	Moment coefficient about $y_h$ -axis (–)
$c_{p_i}$	Pressure coefficient (–)
$F_N$	Total aerodynamic force acting perpendicular to concentrator surface (N)
$F_{N,n}$	Aerodynamic force acting normal to sub-surface $n$ (N)
$F_x$	Drag force (N)
$F_z$	Lift force (N)
$I_u$	Longitudinal turbulence intensity (%)
$I_v$	Lateral turbulence intensity (%)
$I_w$	Vertical turbulence intensity (%)
$l_{eddy}$	Characteristic length of an eddy in the turbulent wind flow (m)
$l_{px_h,n}$	Distance to center of pressure of sub-surface $n$ in $x_h$ -direction (m)
$l_{py_h,n}$	Distance to center of pressure of sub-surface $n$ in $y_h$ -direction (m)
$l_{wind}$	Wavelength of wind speed fluctuation (m)
$l_{x_h}$	Heliostat characteristic length in $x_h$ -direction (m)
$l_{y_h}$	Heliostat characteristic length in $y_h$ -direction (m)
$M_{x_h}$	Aerodynamic moment about $x_h$ -axis (N m)
$M_{y_h}$	Aerodynamic moment about $y_h$ -axis (N m)
$p_i$	Net differential pressure at tap location $i$ (Pa)
$p_i^{back}$	Pressure on lower concentrator surface at tap location $i$ (Pa)
$p_i^{front}$	Pressure on upper concentrator surface at tap location $i$ (Pa)
$p_n$	Mean net differential pressure on concentrator sub-surface $n$ (Pa)
$S_{c_L}$	Spectrum of load coefficient $c_L$ (1/Hz)
$S_u$	Longitudinal wind spectrum ( $(\text{m/s})^2/\text{Hz}$ )
$S_v$	Lateral wind spectrum ( $(\text{m/s})^2/\text{Hz}$ )
$S_w$	Vertical wind spectrum ( $(\text{m/s})^2/\text{Hz}$ )
$T$	Period duration of wind speed fluctuation (s)
$u$	Longitudinal wind speed component (m/s)
$u_*$	Friction velocity (m/s)
$v$	Lateral wind speed component (m/s)
$w$	Vertical wind speed component (m/s)
$x_h$	Horizontal concentrator axis (m)
$y_h$	Vertical concentrator axis (m)

$z$	Height above ground (m)
$z_0$	Roughness length (m)
$z_h$	Axis orthogonal to concentrator; Optical axis (m)
2D	Two-dimensional
3D	Three-dimensional
PMS	Pressure measurement system
RHP	Region of highest pressure coefficients
SAT	Ultrasonic anemometer
$\kappa$	von Karman constant (–)
$ X_{a,L} ^2$	Aerodynamic admittance of load component $L$ (–)
$\bar{\alpha}$	Mean vertical angle of attack; Elevation angle ( $^\circ$ )
$\bar{\beta}$	Mean horizontal angle of attack ( $^\circ$ )
$\rho$	Air density ( $\text{kg/m}^3$ )
$\sigma_u$	Standard deviation of longitudinal wind speed (m/s)
$\sigma_v$	Standard deviation of lateral wind speed (m/s)
$\sigma_w$	Standard deviation of vertical wind speed (m/s)

be modeled comparatively large in relation to the simulated wind conditions, i.e. the simulated boundary layer in a wind tunnel. In other terms, the scaling ratios of the heliostat model and the simulated boundary layer mismatch. By that, the wind tunnel turbulence characteristics at heliostat height differ from the natural, full-scale characteristics. One effect is that in wind tunnel studies, the most energy containing eddies have different sizes compared to the heliostat than in full-scale conditions. Overall, these scaling difficulties leave uncertainties for wind loads determined in wind tunnel studies (Emes et al., 2021). Therefore, it is important to complement wind tunnel studies by investigations at full-scale, taking into account the real-scale heliostat within the natural atmospheric boundary layer (Emes et al., 2021). However, until now, full-scale measurement campaigns have not been conducted or reported often which is most likely due to the relatively great effort and costs at which full-scale studies come. The setup of large heliostats with measurement devices is cumbersome and ensuring suitable wind conditions is time-consuming. As only little full-scale data is yet available, and its collection used to be cumbersome, the main objectives of this study were: (1) to develop a measurement system and a method which allows pressure measurements of real-scale heliostats with minimized effort and (2) to present a first set of full-scale data taken at a  $48.5 \text{ m}^2$  pentagonal Stellio heliostat, which gives insight into the aerodynamics of a real-scale heliostat.

This paper is organized as follows. In Section 2, the experimental method of the conducted field study is presented, including an introduction to the newly developed pressure measurement system, and details on the wind and pressure measurements. In Section 3, the results are presented and discussed which comprise pressure distributions, load coefficients and aerodynamic admittance functions. A final summary and conclusion is presented in Section 4.

## 2. Experimental method

The conducted field study included simultaneous wind and pressure measurements of a pentagonal Stellio heliostat which was installed on the heliostat testing platform (HeliTep) at the DLR site in Juelich. Further information on the HeliTep and the Stellio heliostat can be found in Blume et al. (2020), Balz et al. (2016) or Nieffer et al. (2019). The wind and pressure data was recorded over several individual 10-minute measurement periods. Each of the 10-minute periods was evaluated separately and the data processing is explained in the following sections. Note that a 10-minute time period was chosen to capture a sufficient portion of the wind's turbulence spectrum and at the same time allowing to collect a reasonably great amount of measurement periods. The turbulence spectrum is of particular interest

scales, representing the sizes of the most energy containing eddies in a turbulent flow, were studied and found to affect heliostat wind load coefficients e.g. by Jafari et al. (2019), Emes et al. (2017) and Pfahl (2018).

In particular with regard to the dependency of wind load coefficients on turbulence characteristics (i.e. the turbulence intensity and the integral length scales), a drawback of heliostat wind tunnel studies becomes apparent. According to numerous authors such as Banks (2011), Pfahl et al. (2015) and Jafari et al. (2019), heliostats must

**Table 1**  
Anemometer specifications and mounting setup.

Anemo- meter	Wind- field	Mounting height	Sample rate	Wind- mast
1 <sup>a</sup>	3D	2.9 m	20 Hz	portable
2 <sup>b</sup>	2D	4.7 m	4 Hz	portable
3 <sup>a</sup>	3D	6.7 m	20 Hz	portable
4 <sup>b</sup>	2D	10.3 m	4 Hz	fixed

<sup>a</sup>Gill Instruments *WindMaster* 1590-PK-020/W.

<sup>b</sup>Gill Instruments *WindSonic* Option 1 1405-PK-021.

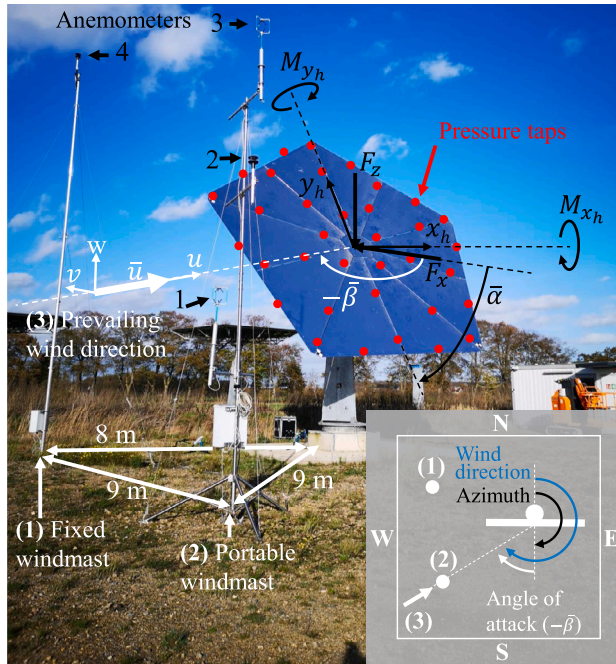


**Fig. 1.** Wind mast and anemometer setup at the Stellio heliostat during measurement periods of this study. Further information on the four anemometers (1–4) is summarized in Table 1.

as it is associated with rapid wind speed fluctuations that lead to significant loads on a structure. The turbulent fluctuations correspond to time periods in the order of seconds to minutes, up to approximately 10 min (Stull, 1988) which is therefore the time period chosen in this study.

## 2.1. Wind measurements

The wind speed and direction of the approaching wind was measured by four ultrasonic anemometers (SATs) at four different heights. Three anemometers were mounted on a portable wind mast which was positioned in front of the Stellio according to the prevailing wind direction (south-west to west). The fourth anemometer was mounted to a fixed wind mast which was installed close to the portable wind mast. Table 1 summarizes the anemometer setup and the mounting heights. Furthermore, Fig. 1 clarifies the positions of the wind masts relative to the Stellio. Note that during mounting of the SATs, the SATs have to be oriented in a certain way, typically towards north, in order to set the SAT coordinate system and to later derive the wind direction relative to north. The mounting of anemometers 1 and 3 could be verified through a compass but an uncertainty of approximately 5° (estimated) remained, i.e. the later stated angles of attack are associated with an uncertainty of 5°.

### 2.1.1. Wind data processing

As mentioned earlier, several individual 10-minute measurement periods were conducted during this field study. For each 10-minute period, the wind data of the four anemometers was processed in the following way: (1) First, each of the four anemometers was evaluated independently by preparing its raw data and determining wind parameters such as the mean wind speed and the turbulence intensity. (2) Second, the wind parameters of all anemometers, corresponding to different heights, were condensed to a single wind parameter set on the elevation axis height of the Stellio.

Regarding step (1): For each of the applied anemometers, the 2D or 3D wind speed recordings were firstly rotated from the SAT coordinate system into the natural wind coordinate system which is aligned with the mean wind direction. In this way, the lateral ( $v'$ ) and vertical ( $w'$ ) wind components contain wind speed fluctuations only and have a zero mean while the longitudinal component comprises the 10-minute mean wind speed  $\bar{u}$  and the longitudinal wind speed fluctuations ( $u'$ ). From the decomposed mean and fluctuating wind speed components, the turbulence intensities  $I_u$ ,  $I_v$  and  $I_w$  were evaluated by means of

$$I_u = \frac{\sigma_u}{\bar{u}} \quad I_v = \frac{\sigma_v}{\bar{u}} \quad I_w = \frac{\sigma_w}{\bar{u}} \quad (1)$$

in which  $\sigma_u$ ,  $\sigma_v$  and  $\sigma_w$  are the standard deviations of the wind speed fluctuations.

Furthermore, the power spectral densities of the fluctuating wind speed components  $S_u$ ,  $S_v$  and  $S_w$ , also simply termed the wind spectra, were derived by transforming the fluctuating wind speed components into the frequency domain.<sup>1</sup>

Lastly, the mean angles of attack were evaluated under which the mean wind speed approached the Stellio. The mean vertical angle of attack  $\bar{\alpha}$  was determined by the elevation angle of the Stellio which was set to  $\bar{\alpha} = 60^\circ$ , i.e. a rather vertical position of the concentrator as seen in Fig. 1. The mean horizontal angle of attack  $\bar{\beta}$  was calculated by subtracting the mean wind direction from the heliostat's azimuth angle. Summarizing the first evaluation step, for each 10-minute measurement period, four sets of wind parameters were determined according to the applied anemometers and their corresponding heights. Next, these multiple sets of wind parameters had to be condensed to a single set of wind parameters corresponding to the elevation axis height of the Stellio. The elevation axis height of the Stellio as installed on the HeliTep is approximately 5.7 m for an elevation angle of  $60^\circ$ .

Regarding step (2): The mean wind speed on elevation axis height was interpolated from the various mean wind speeds on different heights by fitting Prandtl's logarithmic law to the data. In this way, also the roughness length  $z_0$  could be estimated which is a measure of the terrain roughness of the site, here the HeliTep. Adopted from Holmes (2015), the Prandtl logarithmic law reads

$$\bar{u}(z) = \frac{u_*}{\kappa} \ln \left( \frac{z}{z_0} \right) \quad (2)$$

where  $\kappa = 0.4$  is the von Karman constant,  $u_*$  is the friction velocity and  $z_0$  is the roughness length.

In a similar way, the turbulence intensities on elevation axis height were evaluated through interpolation. According to Holmes (2015), they can be defined as a function of the height above ground as follows:

$$I_u(z) = \frac{1}{\ln \left( \frac{z}{z_0} \right)} \quad I_v(z) = \frac{0.88}{\ln \left( \frac{z}{z_0} \right)} \quad I_w(z) = \frac{0.55}{\ln \left( \frac{z}{z_0} \right)} \quad (3)$$

The scaling factors of 1, 0.88 and 0.55 have been empirically derived through dedicated field studies in the past (Holmes, 2015). Note that during this study, aforementioned scaling factors did not match the measured 10-minute turbulence intensities well, most likely due to differences in the terrain and boundary layer conditions compared to

<sup>1</sup> The wind spectra were determined by using Matlab's *pwelch* function with default settings.



the field studies mentioned in Holmes (2015). Therefore, the scaling factors were kept variable during the fitting process.

Furthermore, the mean horizontal angle of attack  $\bar{\beta}$  on elevation axis height had to be determined and was averaged from the measured angles of attack at anemometers 1 and 3.

Lastly, the wind spectra on elevation axis height had to be defined. To avoid an interpolation between the measured spectra, it was concluded to evaluate the wind spectra of the closest 3D anemometer to the elevation axis height of the Stellio which was anemometer 3. Hence, the wind spectra evaluated in this study have not been measured exactly on elevation axis height but, due to the mounting height of anemometer 3, at approximately 1.2 times the elevation axis height.

In summary, for each 10-minute measurement period, a set of wind parameters (mean wind speed, turbulence intensities, angles of attack, wind spectra) corresponding to the elevation axis height of the Stellio was evaluated.

## 2.2. Pressure measurements

The pressure distribution over the surface of the Stellio concentrator was measured through a newly developed pressure measurement system (PMS) which particularly meets the requirements of field measurements of real-scale heliostats or other large-scale structures.

### 2.2.1. Pressure measurement system

The unique feature of the PMS is that there is no need of connecting the desired pressure taps to a single data acquisition system but instead, a variable amount of small measurement boxes is used that are self-sufficient and can be placed right next to the pressure taps as depicted in Fig. 3(a). In this way, long tubing from the pressure taps to the data acquisition system is avoided which is impractical for large-scale structures and could cause significant loss of pressure quality. The core component of each box is a Sensirion differential pressure sensor, type SDP810-500Pa with a measurement range of  $\pm 500$  Pa and a specified accuracy of 3 % of reading. The SDP810-type pressure sensor is based on a thermal measurement principle, i.e. the sensor initially measures a temperature gradient between two heating elements that are surpassed by the air flow which is induced by the pressure gradient (Sensirion, 2017). The sensor then translates the measured temperature gradient into the respective differential pressure. This sensor-internal translation is only valid for such ambient pressure for which the sensor was calibrated ( $p_{amb,calib} = 966$  mbar). If the ambient pressure during the measurement period ( $p_{amb}$ ) differs, which is often the case, the exported differential pressures ( $p_{diff,raw}$ ) have to be corrected during post-processing according to the true ambient pressure. Therefore, each measurement box contains an Amsys ambient pressure sensor, type AMS6915-1200-B-H-3 with a measurement range of 750 to 1200 mbar and a specified accuracy of 0.5% of full span output. Such ambient pressure is used to correct the exported differential pressure through the formula  $p_{diff} = p_{diff,raw} \frac{p_{amb,calib}}{p_{amb}}$  where  $p_{diff}$  is the corrected differential pressure (Sensirion, 2017).

While each single box is self-sufficient, they all communicate via a master-slave configuration using radio transmission. In order to synchronize the boxes (i.e. to provide a synchronous time stamp for all pressure signals), real-time-clocks (RTC) are integrated in each box which are triggered by the master at the exact same time and therefore set their internal time to the same reference. Likewise, a trigger from the master is used to start recording data in each box at the exact same time. Further components of each box are a microprocessor, an SD-card to store the data and a battery. The battery lasts between 6 to 8 h continuous measurement time which is sufficient for one-day field measurements. The maximum sample rate of the PMS is 50 Hz and was applied for the measurements of this study. One last aspect to be mentioned is that the boxes of the PMS are not fully water-proof so the chances of rain should be low during a measurement period to avoid damage to the PMS but also to avoid a clogging of the pressure taps.

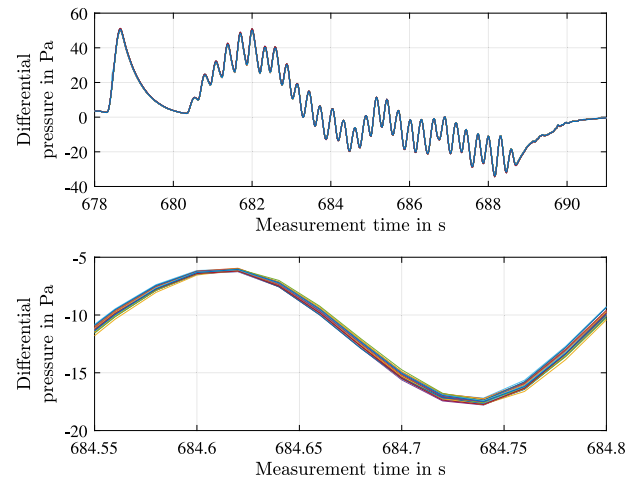


Fig. 2. Laboratory test of pressure measurement system. Overlay of 35 pressure signals to verify synchronization of measurement boxes.

Due to the same reason, it is not recommended to keep the PMS outside during night but the boxes rather have to be attached in the morning and detached in the evening which adds to the total time required for a measurement campaign.

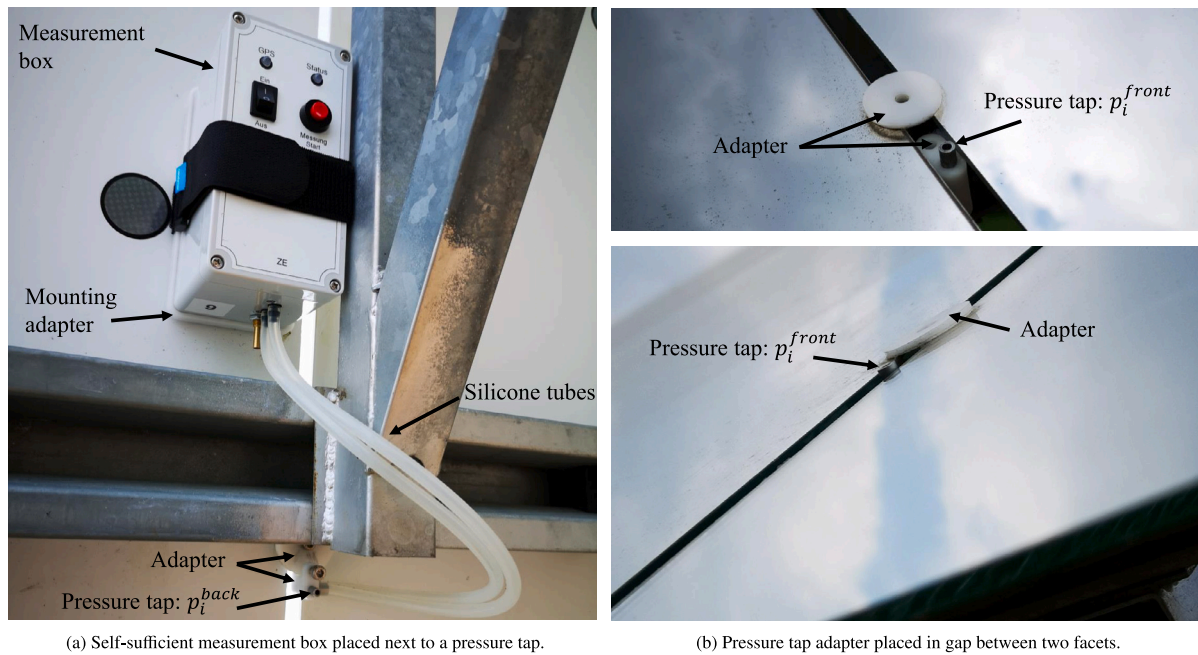
Pre-tests of the PMS have been carried out in the laboratory to check the proper synchronization of all boxes. Therefore, all boxes (35 in this case) have been connected to a large container to which pressure was applied manually and randomly. The two objectives of this test were to verify (1) that all boxes start recording data at the same time and (2) that the time stamps, produced by the RTCs, stay synchronous over a measurement time of approximately 10 min. The latter aspect had to be investigated because the paces of all RTCs are expected to vary slightly. The result of the pre-test is shown in Fig. 2. An overlay of all 35 pressure signals after roughly 10 min is depicted and proves that all pressure signals are synchronous. In further lab tests of approximately 6 h continuous measurement time, a slight deviation between the pressure signals could be noticed and a maximum shift of approximately 9  $\mu$ s/s could be evaluated. In this study, with a maximum measurement time of 600 s, the maximum deviation towards the end of the measurement period is therefore less than 0.006 s which is considered negligibly small.

### 2.2.2. Measurement setup at Stellio heliostat

In case of the Stellio, the 35 measurement boxes have been applied to the concentrator using adapter plates with an elastic band for quick attachment and detachment as depicted in Fig. 3(a). The approximate positions of the boxes are indicated in Fig. 1, while in Fig. 4(a), the coordinates are given in the concentrator coordinate system. The tap positions have been measured at the real-scale heliostat and must be stated with an uncertainty of 1 cm, i.e. the true tap position is expected within a radius of 1 cm about the given position. Furthermore, Fig. 3(b) depicts the adapter that was used to realize the pressure tap. The tap has an inner diameter of 3 mm and is connected to the measurement box via silicon tubes of 40 cm length with an inner diameter of 3 mm. To avoid drilling holes into the facets, most of the tap adapters were placed in between the small gaps of two facets and a few ones right at the edges of the facets. As the gap between two facets is less than 1 cm wide and therefore very small compared to the entire concentrator, the impact of the gaps on the flow over the concentrator was considered negligibly small.

### 2.2.3. Data processing

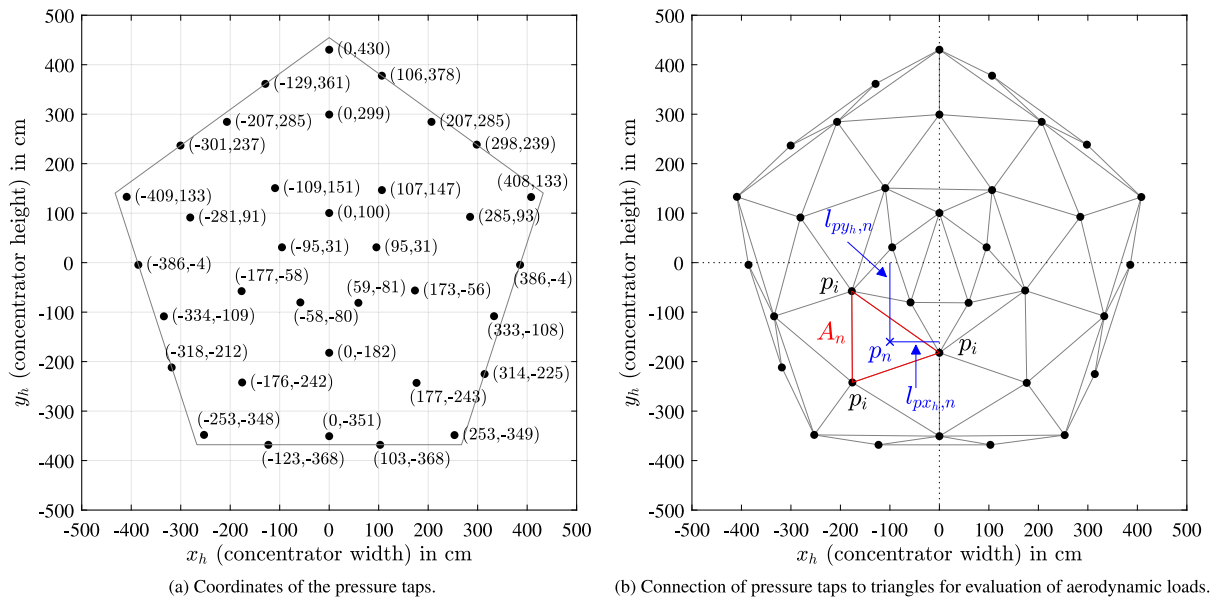
At each pressure tap  $i$ , the differential pressure  $p_i$  was measured, representing the net pressure between the concentrator front and back



(a) Self-sufficient measurement box placed next to a pressure tap.

(b) Pressure tap adapter placed in gap between two facets.

Fig. 3. Setup and application of the pressure measurement system.



(a) Coordinates of the pressure taps.

(b) Connection of pressure taps to triangles for evaluation of aerodynamic loads.

Fig. 4. Distribution of pressure taps over the Stello concentrator surface.

side  $p_i = p_i^{front} - p_i^{back}$ . Together, the net pressures of all pressure taps define a net pressure distribution  $p(x_h, y_h)$ . To determine the wind-induced aerodynamic loads, the net pressure distribution was integrated over the heliostat's concentrator surface, similar to the procedure and the equations described in Emes et al. (2019). The integration was performed on the mean pressure distribution to determine the mean loads as well as on the instantaneous pressure distributions for each time step to determine the time course of the aerodynamic loads. To integrate the pressure distribution, the concentrator surface was divided into sub-surfaces which were defined through triangulation between the pressure taps. Fig. 4(b) depicts how the  $i = 35$  pressure taps have been connected to  $n = 53$  triangles. Each triangle therefore defines the sub-surface  $A_n$  where a net resultant pressure  $p_n$  applied, calculated from the three corner pressures as  $p_n = \frac{1}{3} \sum p_i$ . The force  $F_{N,n}$  acting

normal to the sub-surface was then derived by

$$F_{N,n} = \iint p(x_h, y_h) dx_n dy_n = A_n p_n \quad (4)$$

which acts in the center of pressure of the sub-surface. The position of the center of pressure in  $x_h$ - and  $y_h$ -direction was calculated by

$$l_{px_h,n} = \frac{\iint x_h p(x_h, y_h) dx_n dy_n}{\iint p(x_h, y_h) dx_n dy_n} = \frac{\iint x_h p(x_h, y_h) dx_n dy_n}{F_{N,n}} \quad (5)$$

$$l_{py_h,n} = \frac{\iint y_h p(x_h, y_h) dx_n dy_n}{\iint p(x_h, y_h) dx_n dy_n} = \frac{\iint y_h p(x_h, y_h) dx_n dy_n}{F_{N,n}} \quad (6)$$

The total aerodynamic force, acting perpendicular to the entire concentrator is the sum of all triangles and was calculated by

$$F_N = \sum p_n A_n \quad (7)$$

Moreover,  $F_N$  can be divided into the drag force  $F_x$  and the lift force  $F_z$  by means of the elevation angle  $\bar{\alpha}$  as follows:

$$F_x = F_N \sin \bar{\alpha} \quad (8)$$

$$F_z = F_N \cos \bar{\alpha} \quad (9)$$

The total aerodynamic moments about the concentrator  $x_h$ - and  $y_h$ -axis were calculated by the sum over all triangles which read

$$M_{x_h} = \sum F_{N,n} l_{py_h,n} \quad (10)$$

$$M_{y_h} = \sum F_{N,n} l_{px_h,n} \quad (11)$$

As the wind speed varied during the different measurement periods and the measured net pressures and loads are not directly comparable, they were normalized with respect to the specific conditions during each period. Such normalization results in non-dimensional coefficients which can then be easily compared and analyzed. The net pressure coefficient was calculated by

$$c_{p_i} = \frac{p_i}{\frac{\rho}{2} \bar{u}^2} \quad (12)$$

where  $\rho$  is the air density and  $\bar{u}$  the 10-minute mean wind speed at elevation axis height.

The aerodynamic force and moment coefficients were calculated by

$$c_{F_x} = \frac{F_x}{\frac{\rho}{2} \bar{u}^2 A} \quad c_{F_z} = \frac{F_z}{\frac{\rho}{2} \bar{u}^2 A} \quad (13)$$

$$c_{M_{x_h}} = \frac{M_{x_h}}{\frac{\rho}{2} \bar{u}^2 A l_{y_h}} \quad c_{M_{y_h}} = \frac{M_{y_h}}{\frac{\rho}{2} \bar{u}^2 A l_{x_h}} \quad (14)$$

where  $A$  is the concentrator area and  $l_{x_h}$  and  $l_{y_h}$  are the characteristic lengths in  $x_h$ - and  $y_h$ -direction, respectively. The concentrator area of the Stellio is  $A = 48.5 \text{ m}^2$  and the characteristic length was defined to be  $l_{x_h} = l_{y_h} = \sqrt{A} \approx 6.96 \text{ m}$ .

Moreover, the aerodynamic admittance functions were calculated from the measured data. The aerodynamic admittance is important when analyzing wind-induced *dynamic* loads on a structure. While the mean approaching wind causes static loads, the changes in wind speed due to turbulence cause fluctuating loads, i.e. dynamic loads on the structure. The link between the wind speed fluctuations and the dynamic load is called the aerodynamic admittance and is defined within the frequency domain. Towards low frequencies, the aerodynamic admittance tends towards unity while for larger frequencies it decreases significantly. Such behavior can be explained as follows. The turbulent wind can be imagined as a superposition of different size eddies where small eddies correspond to high frequencies and vice versa. Those eddies which are small compared to the structure only cover and act on a small area of the surface simultaneously, thus their spatial correlation is reduced (Petersen and Werkle, 2017; Dyrbye and Hansen, 1999). As a consequence, small eddies are less effective in inducing loads on a structure which is accounted for by the decrease of the aerodynamic admittance. On the other hand, eddies that are of similar size than the structure and larger engulf the entire structure and are thus more effective in inducing loads. Therefore, the admittance tends towards unity for low frequencies.

The aerodynamic admittance is typically depicted over a non-dimensional frequency  $n = f l / \bar{u}$  where  $f$  is the dimensional frequency,  $l$  is a characteristic length of the structure and  $\bar{u}$  is the mean wind speed. This normalization reflects the relation of the structure size to the eddy size. As aforementioned, the turbulent wind consists of many different size eddies which together travel with the mean wind flow  $\bar{u}$  (Stull, 1988). At a defined point in space (e.g. a wind sensor), the turbulent wind leads to wind speed fluctuations of different period durations  $T$  (or frequencies  $f = 1/T$ ) where in general, the large eddies lead to longer lasting fluctuations (larger  $T$ , lower  $f$ ) than the smaller eddies (shorter  $T$ , higher  $f$ ). Through the mean wind speed  $\bar{u}$ , the spatial

expansion, i.e. the wavelength of a certain wind speed fluctuation can be calculated by  $l_{wind} = \bar{u} T = \bar{u} / f$  (Stull, 1988; Kwok, 2013). When interpreting the wavelength as the eddy size, the previously introduced non-dimensional frequency  $n = f l / \bar{u} = l / l_{wind}$  takes on a value of 1 if the eddy size is in the same range as the size of the structure (Pfahl et al., 2015). However, approximating the eddy size by the wavelength is only a vague approximation. To better estimate the eddy size, it would be necessary to measure the wind speed at different locations that are a certain distance apart and then correlate the wind measurements (Hucho, 2011). This procedure was not applied during this study but measurement results reported in literature suggest that the frequency  $f$  of a certain wind speed fluctuation correlates with the size of the eddy  $l_{eddy}$  that causes the fluctuation as follows:  $f l_{eddy} / \bar{u} = C$  where  $C$  is a constant lying between 0.09 and 0.15 (Hucho, 2011; Ruscheweyh, 1982). These results indicate that the non-dimensional frequency  $n$  takes on a value of approximately 0.1 if the eddy size is in the same range as the structure size. Overall, it shall be emphasized that measuring or estimating the sizes of eddies in the turbulent wind is rather difficult. In this study, based on aforementioned explanations, a non-dimensional frequency  $n$  between approximately 0.1 and 1 is considered to indicate that the eddy size is similar to the size of the structure, while an exact size of the eddy cannot be stated.

As aforementioned, the aerodynamic admittance links the dynamic load to the fluctuating wind speed in the frequency domain. In more detail, it links the power spectral densities  $S$ , also simply termed spectra, of the wind speed and the dynamic load. An analytical model of the aerodynamic admittance  $|\chi_a(f)|^2$  was derived in Blume et al. (2023) and reads

$$|\chi_{a,L}(f)|^2 = \frac{\bar{u}^2 S_{c_L}(f)}{4 \bar{c}_L^2 S_u(f) + \left(\frac{\partial c_L}{\partial \beta}\right)^2 S_v(f) + \left(\frac{\partial c_L}{\partial \alpha}\right)^2 S_w(f)} \quad (15)$$

in which  $L$  represents the desired aerodynamic load component ( $F_x$ ,  $F_z$ ,  $M_{x_h}$  or  $M_{y_h}$ ),  $S_u$ ,  $S_v$  and  $S_w$  denote the wind spectra and  $S_{c_L}$  describes the spectrum of the dynamic load in non-dimensional form. Moreover,  $\frac{\partial c_L}{\partial \alpha}$  and  $\frac{\partial c_L}{\partial \beta}$  denote the derivatives of the aerodynamic load coefficient with respect to the angles of attack, evaluated at the mean angles of attack of the respective measurement period.

Note that the analytical model as stated in Eq. (15) is generally only valid for rather small values of  $\bar{\beta}$ , see also Blume et al. (2023) for the detailed reasons of this limitation. For the particular case that the  $\left(\frac{\partial c_L}{\partial \alpha}\right)$ -related term in the denominator is negligible, the admittance model is valid for any value of  $\bar{\beta}$ .

#### 2.2.4. Uncertainty estimation of aerodynamic loads

The evaluated and later stated aerodynamic loads of this study are associated with a few uncertainties which shall be briefly explained and estimated in the following.

The pressure sensors were distributed over the concentrator surface of the Stellio with the objective to cover the largest possible reflective surface area. However, along the edges towards the corners, minor areas could not be covered and therefore, the evaluated area was approximately 2.5 % smaller than the total concentrator area. Hence, the determined loads of this study are related to a slightly smaller area and an uncertainty arises regarding the full loads that would apply on the entire concentrator. Under the assumption that the pressures decrease rapidly towards the edges, due to separation, it is concluded that the pressures along the edges are small and do not induce a significant amount of load. Thus, the determined loads (related to the slightly smaller area) are considered approximately equal to the loads of the total area. Even though the validity of the aforementioned explanation is assumed, the later presented loads may be up to 2.5 % larger.

An additional uncertainty arises from the accuracy of the pressure sensors which was previously stated to be 3 %. The impact on the load determination is evaluated by adding a random error between –3 %



and 3 % to all measured pressures and comparing the error-related loads to the reference loads. This procedure is repeated 1000 times, i.e. 1000 slightly different pressure distributions are evaluated and the respective loads are compared to the reference. Finally, a mean error of all 1000 repetitions is calculated in terms of the standard deviation which is then a measure of the uncertainty. For the moments about the  $x_h$ - and  $y_h$ -axis, the uncertainty was found to be 3 % and 1.6%, respectively. For the drag and lift force, the uncertainty was found to be 0.4%.

In a similar way, the impact of varying pressure tap locations was evaluated, which were measured with an uncertainty of approximately 1 cm. Therefore, 1000 slightly different pressure tap configurations were evaluated by adding a random offset between -1 cm and 1 cm to the reference tap locations as stated in Fig. 4(a). The derived uncertainties were negligibly small and did not increase the previously estimated uncertainties associated with the sensor accuracy.

In principal, all aforementioned uncertainties apply to the dimensional loads as well as to the non-dimensional loads, i.e. the load coefficients. Yet, the latter are determined by normalizing the dimensional loads by, amongst other parameters, the square of the mean wind speed which can inherit further uncertainties. During this study, the wind speed was measured approximately 9 m in front of the Stellio which is considered a sufficient distance. Nevertheless, a heliostat constitutes a certain barrier to the wind flow due to which a region of flow stagnation evolves in upstream direction. Therefore, the measured wind speed in this study may not have been the true free stream velocity but a slightly reduced velocity. This effect has not been further analyzed, but could, in principal, lead to slightly increased load coefficients.

### 3. Results and discussion

The results of nine individual 10-minute measurement periods are presented in the following. During each measurement period, the elevation angle  $\bar{\alpha}$  of the Stellio was fixed to 60°. The angle of attack  $\bar{\beta}$  varied between -14° and -66° and will be individually stated for each measurement period. Regarding the sign of  $\bar{\beta}$ , note that an angle of attack of e.g. -60° is usually considered to have the same effect on the concentrator as an angle of attack of +60° due to the (approximate) symmetry of the concentrator about the  $y_h$ -axis. Therefore, when irrelevant, the sign of  $\bar{\beta}$  will not be explicitly stated in the following, but rather absolute values ( $|\bar{\beta}|$ ) will be presented. Likewise, the load coefficients will be presented over positive angles of attack, as it is typically the case.

When investigating aerodynamic loads and in particular when comparing results of different studies (full-scale or wind tunnel studies), it is furthermore important to characterize the investigated boundary layer. A characteristic value of the boundary layer is the roughness length  $z_0$  and is therefore often stated in different studies. As explained in Section 2.1, the roughness length of this study could be estimated from fitting Prandtl's logarithmic law to the 10-minute mean wind speeds at different heights. From the nine investigated measurement periods, the roughness length was averaged and found to be  $z_0 \approx 0.05$  m which agrees well with expected values for a terrain similar to the HeliTep.

A final note shall be given regarding the later stated turbulence intensities of each measurement period. For a given boundary layer with a fixed roughness length  $z_0$ , as it is approximately the case in this study, the overall turbulence level is expected to be rather constant at a certain height above ground (see also Eq. (3)). However, the evaluated turbulence intensities of the 10-minute measurement periods are found to vary significantly, between 22 % and 36 % which could be due to changes in atmospheric stability. Therefore, the later presented turbulence intensities may not be interpreted as representative values of the entire boundary layer but rather as snapshots of the strength of wind speed fluctuations within 10-minute periods of the same boundary layer. It must be further considered that the mean wind speeds varied

amongst the different measurement periods (between 2.6 and 5.7 m/s as also later stated in the captions of Figs. 5(a)–5(i)) so the turbulence intensities have not been determined from equal mean wind speeds which can also lead to differences between the values and may reduce their comparability.

#### 3.1. Mean pressure distributions

Fig. 5 shows the non-dimensional 10-minute mean pressure distributions of the Stellio in descending order of the measured angles of attack  $\bar{\beta}$  (descending order considering  $|\bar{\beta}|$ ). Clearly, it appears that the region of highest pressure coefficients (red area, short: RHP) moves horizontally, i.e. in  $x_h$ -direction, from the edge of the concentrator towards its center when  $|\bar{\beta}|$  decreases from about 66° to 14°. Furthermore, it appears that the maximum  $\bar{c}_p$ -values within the RHPs are very consistent for  $|\bar{\beta}|$  up to 47° and reach values between approximately 2.2 and 2.6. Towards larger angles of attack, the maximum  $\bar{c}_p$ -values then decrease and reach values of approximately 2.0 and 1.6 for  $|\bar{\beta}| = 59^\circ$  and  $|\bar{\beta}| = 66^\circ$ , respectively (Figs. 5(b) and 5(a)). The observed decrease of the  $\bar{c}_p$ -values can be explained by the increasing angles of attack due to which the wind flow is rather parallel, i.e. in line with the concentrator, and the acting pressure is thus reduced.

In contrast to the significant movement in  $x_h$ -direction, the RHP does not notably move in vertical ( $y_h$ ) direction which is due to the constant elevation angle during all measurement periods. The steep elevation angle of 60° causes the RHP to be located slightly below the concentrator  $x_h$ -axis in all cases, forming a nearly symmetrical pressure distribution about the  $x_h$ -axis.

The pressure distributions of this study are in very close agreement with results of a wind tunnel study conducted by Emes et al. (2019) who present, amongst many other results, the mean pressure distributions of a rectangular heliostat model with an elevation angle  $\bar{\alpha} = 60^\circ$  and angles of attack  $\bar{\beta} = 0^\circ$  and  $\bar{\beta} = 60^\circ$ . The parameters of the simulated turbulent boundary layer were stated to be  $z_0 = 0.03$  m and  $I_u = 13$  % at elevation axis height. The results of the wind tunnel study show that with increasing  $|\bar{\beta}|$ , the RHP moves horizontally from the center of the concentrator towards the edge. At the same time, no significant movement can be observed in vertical direction. The  $\bar{c}_p$ -values within the RHP were found to be approximately 2.0 for  $\bar{\beta} = 0^\circ$  and 2.5 for  $\bar{\beta} = 60^\circ$ . Compared hereto, the  $\bar{c}_p$ -value of this field study for  $\bar{\beta}$  close to 0° is 10 % higher (2.2 at  $|\bar{\beta}| = 14^\circ$ ). On the other hand, for  $\bar{\beta}$  close to 60°, the  $\bar{c}_p$ -value of this study is approximately 20 % smaller (2.0 at  $|\bar{\beta}| = 59^\circ$ ) than the wind tunnel result. Note that due to the different shapes of the investigated heliostats (rectangular in wind tunnel study, pentagonal in this field study), the pressure distribution can evolve slightly differently. In particular, the decrease of the  $\bar{c}_p$ -values for larger angles of attack may not be associated with the exact same angle of attack. In fact, in case of the here investigated pentagonal concentrator, the  $\bar{c}_p$ -values appear to decrease after  $|\bar{\beta}| \approx 50^\circ$ . On the other hand, in the wind tunnel study, the  $\bar{c}_p$ -values do not seem to decrease before  $\bar{\beta} = 60^\circ$ . Thus, the wind tunnel  $\bar{c}_p$ -value of 2.5 for  $\bar{\beta} = 60^\circ$  may as well be comparable to the field study  $\bar{c}_p$ -values of  $\bar{\beta} < 60^\circ$ . In that case, the wind tunnel result ( $\bar{c}_p = 2.5$ ) and the field study results ( $\bar{c}_p = 2.2 - 2.6$ ) agree well.

In overall conclusion, the observed behavior of the RHP is very consistent between the two studies. Moreover, the pressure coefficients of the wind-tunnel study lie within the same range as the field-study coefficients. Remaining deviations in the  $\bar{c}_p$ -values are presumably related to the different turbulent boundary layers of the two studies where the overall turbulence level of this study was higher.

#### 3.2. Aerodynamic load coefficients

From the previously presented mean pressure distributions, the mean aerodynamic force and moment coefficients have been determined according to Eqs. (4)–(14). Figs. 6(a) and 6(b) show the calculated mean drag and lift force coefficients over the angle of attack  $\bar{\beta}$

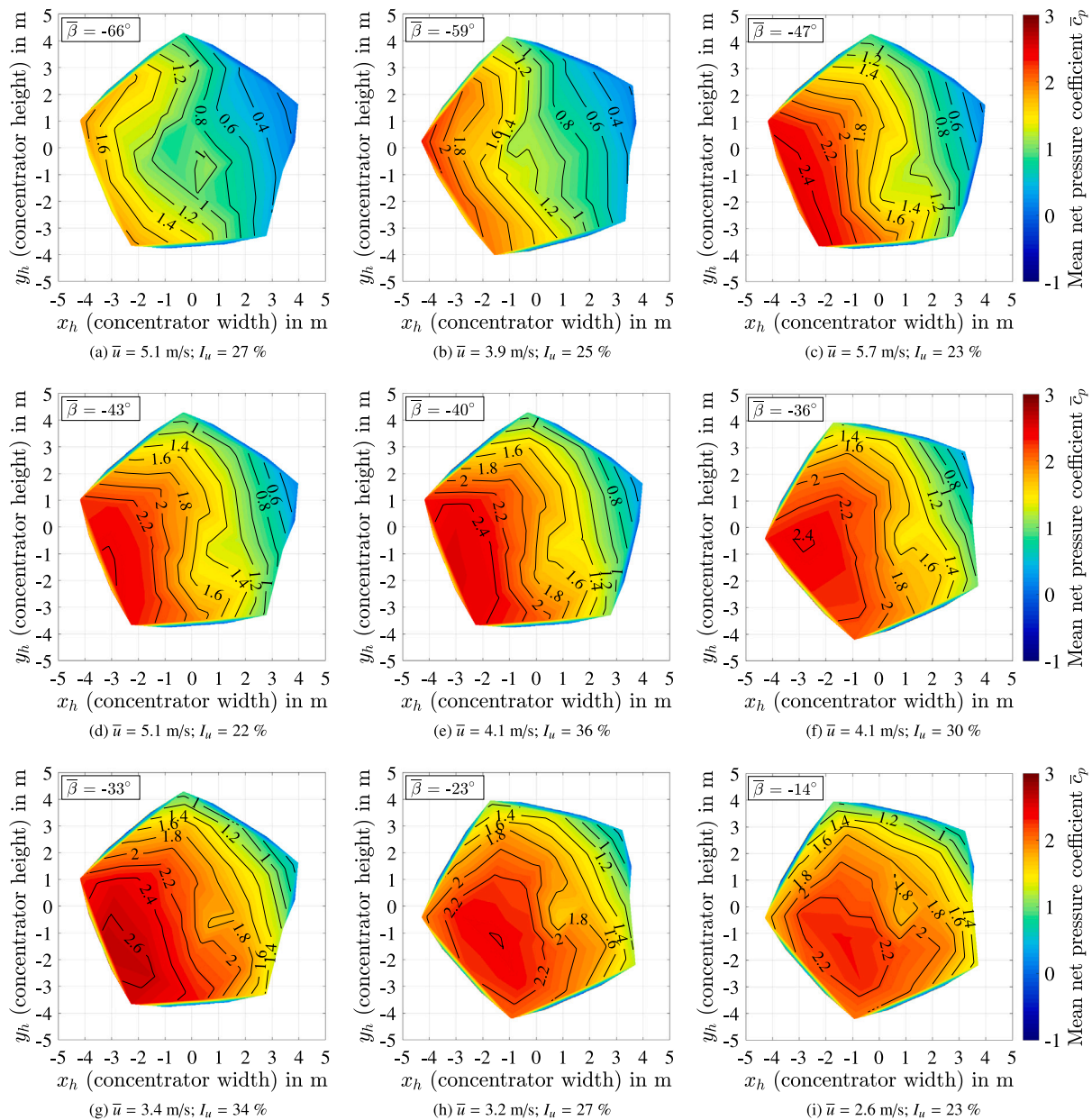


Fig. 5. Distribution of the 10-minute mean net pressure coefficient  $\bar{c}_p$  over the Stello concentrator surface. The mean wind speed and turbulence intensity of each period is stated in the respective caption. (For interpretation of the references to color in this figure legend, the reader is referred to the web version of this article.)

while the turbulence intensity  $I_u$  during the 10-minute period is indicated in terms of a color scale. Both the mean drag and lift coefficients follow a similar trend over  $\bar{\beta}$ , remaining almost constant up to an angle of attack of  $30^\circ$ , and decreasing afterward. This behavior can be explained as follows. At small angles of attack, the wind approaches the heliostat almost head on and the drag as well as the lift is thus maximized. With increasing angles of attack, the orientation of the wind flow relative to the heliostat changes from perpendicular to rather parallel so the drag and lift is reduced, as was already concluded from the mean pressure distributions. This consequently leads to a decrease of the force coefficients.

In addition to the force coefficients, Fig. 7 shows the mean moment coefficients related to the concentrator  $x_h$ - and  $y_h$ -axis over the angle of attack  $\bar{\beta}$  and with  $I_u$  given in terms of a color scale. Considering Fig. 7(a), the course of  $\bar{c}_{M_{xh}}$  over the angle of attack is similar to the courses of  $\bar{c}_{F_x}$  and  $\bar{c}_{F_z}$ . With regard to the previous explanations, for very small angles of attack, the force acting normal to the concentrator is maximized. In combination with the inclined concentrator and the

resulting shift of the RHP below the  $x_h$ -axis, the moment about the  $x_h$ -axis reaches its maximum value for small angles of attack. According to Fig. 7(a), the maximum moment coefficient  $\bar{c}_{M_{xh}}$  reaches a value between 0.06 and 0.07 for an elevation angle of  $60^\circ$ . With increasing angles of attack  $\bar{\beta}$ , the force acting normal to the concentrator then decreases while the distance of the RHP to the  $x_h$ -axis remains almost constant. In total, the moment about the  $x_h$ -axis decreases continuously for higher angles of attack due to the reduced aerodynamic force.

A different behavior can be observed for the moment coefficient about the  $y_h$ -axis. In Section 3.1, it was already discussed that the RHP significantly moves in horizontal direction with varying angles of attack, hence its distance to the center varies. In turn, this leads to a strong variation of the moment about the  $y_h$ -axis. For very small angles of attack, the pressure distribution is very symmetric about the  $y_h$ -axis and no significant moment is created. With increasing angles of attack, the pressure distribution becomes asymmetric about the  $y_h$ -axis, i.e. the RHP moves towards the concentrator edge and leads to an increase of the moment coefficient. In case of the Stello heliostat, a



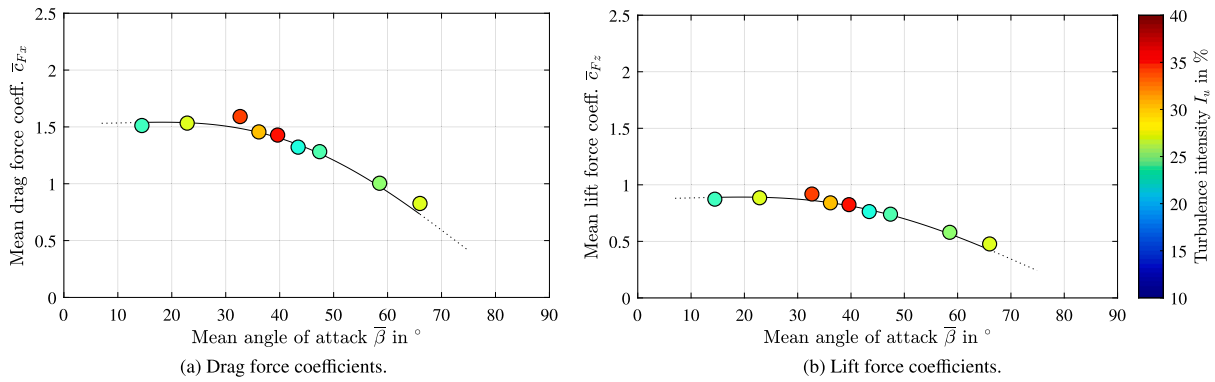


Fig. 6. 10-minute mean force coefficients over the mean angle of attack  $\bar{\beta}$  at an elevation angle  $\bar{\alpha} = 60^\circ$ . (For interpretation of the references to color in this figure legend, the reader is referred to the web version of this article.)

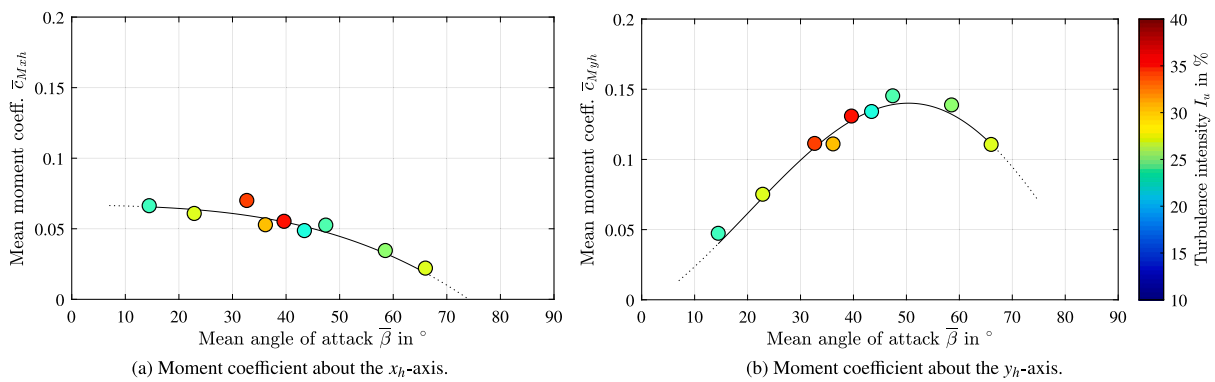


Fig. 7. 10-minute mean moment coefficients over the mean angle of attack  $\bar{\beta}$  at an elevation angle  $\bar{\alpha} = 60^\circ$ . (For interpretation of the references to color in this figure legend, the reader is referred to the web version of this article.)

maximum moment about the  $y_h$ -axis is observed at an angle of attack of approximately  $50^\circ$ . Greater angles of attack than  $50^\circ$  then lead to a decrease of  $\bar{c}_{M_{yh}}$  again which is due to the reduced force acting normal to the concentrator at higher angles of attack.

With regard to the turbulence intensities, Figs. 6 and 7 indicate that the mean coefficients of neither the forces nor the moments significantly vary with the measured 10-minute turbulence intensities even though, in general, a dependency was expected, as stated in Section 1. Presumably, this is due to aforementioned reason that the overall turbulence level on elevation axis height is rather constant while the measured 10-minute turbulence intensities must be treated as snapshots and are not representative for the entire boundary layer. However, the impact of the 10-minute turbulence intensities on the mean load coefficients shall be further investigated in the future by taking more measurement periods into account.

### 3.3. Aerodynamic admittance functions

The aerodynamic admittance function links the fluctuating aerodynamic load to the fluctuating approaching wind. Hence, it provides information on the mechanisms that induce aerodynamic loads on a heliostat. From the admittance model in Eq. (15), it becomes apparent that the wind speed fluctuations in all three directions, represented by the longitudinal  $S_u$ , lateral  $S_v$  and vertical  $S_w$  wind spectrum, can possibly contribute to the dynamic load on a heliostat. However, it is strongly dependent on the investigated load component how much the different wind spectra contribute. More precisely, the non-dimensional load coefficient and its course over the elevation angle and angle of attack, represented by the derivatives  $\frac{\partial c_L}{\partial \alpha}$  and  $\frac{\partial c_L}{\partial \beta}$ , determine the contribution of each wind spectrum. For example, taking the aerodynamic

moment  $M_{yh}$  into account, for very small and very large angles of attack, the coefficient  $\bar{c}_{M_{yh}}$  is close to zero, thus the term  $4\bar{c}_{M_{yh}}^2$  is close to zero. On the other hand, the derivative  $\frac{\partial c_{M_{yh}}}{\partial \beta}$  is relatively large, approximately between 0.2 and 0.3. Hence, the term  $(\frac{\partial c_{M_{yh}}}{\partial \beta})^2$  is comparably large and it can be expected that the lateral wind spectrum  $S_v$  has a greater impact on the fluctuating moment about the  $y_h$ -axis than the longitudinal wind spectrum  $S_u$  for very small and large angles of attack. In contrast, the fluctuating moment about the  $x_h$ -axis,  $M_{xh}$ , as well as the fluctuating drag and lift forces,  $F_x$  and  $F_z$ , are expected to be much less dependent on the lateral wind spectrum  $S_v$  for angles of attack up to approximately  $30^\circ$  as the courses of their coefficients are almost constant over  $\bar{\beta}$  and thus their derivatives  $\frac{\partial c_L}{\partial \beta}$  are small.

The impact of the vertical wind spectrum  $S_w$  can be discussed in the same way, taking the derivative  $\frac{\partial c_L}{\partial \alpha}$  into account. However, in this study too little data is available to investigate the dependency of coefficients on varying elevation angles. Therefore,  $\frac{\partial c_L}{\partial \alpha}$  cannot be evaluated and only the impact of  $S_u$  and  $S_v$  will be discussed in the following.

#### 3.3.1. Admittance function of drag force

Fig. 8 shows the admittance function of the drag force  $F_x$  determined from the results of the various 10-minute measurement periods of this study. The admittance function is depicted over the non-dimensional frequency  $n = f \frac{l}{u}$  where the characteristic length of the here investigated Stello is  $l = 6.96$  m, see also Section 2.2.3. The mean angle of attack  $|\bar{\beta}|$  during each measurement period is depicted in terms of a color scale. Furthermore, a mean admittance function is shown in black which is simply defined as the average of all individual

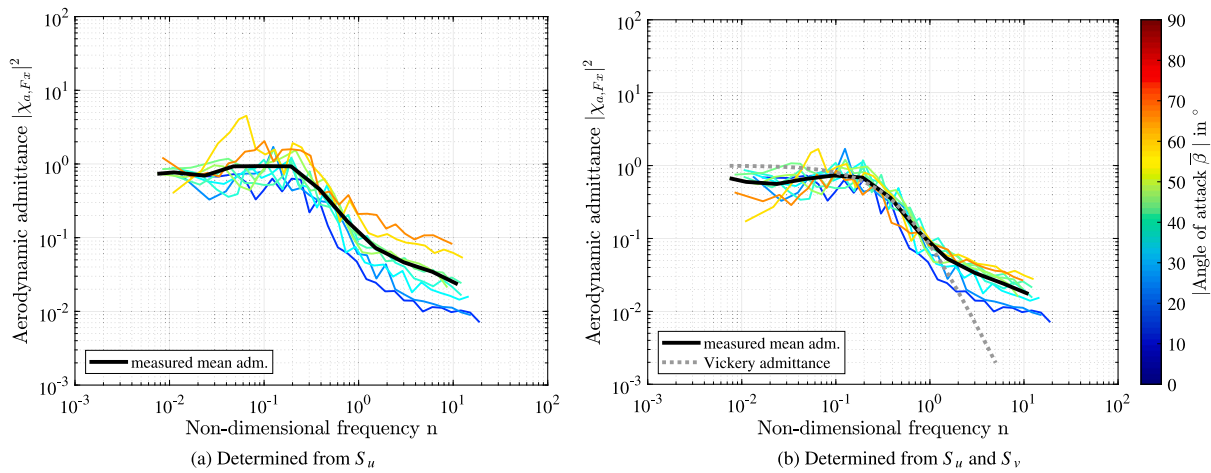


**Fig. 8.** Aerodynamic admittance functions of the drag force  $F_x$ . Impact of  $S_w$  assumed negligible. Therefore, depicted admittances in (b) are considered in their final state. (For interpretation of the references to color in this figure legend, the reader is referred to the web version of this article.)

admittance functions. For comparison purposes, the gray dashed line in Fig. 8(b) represents the widely known Vickery admittance function which has been determined for flat plates perpendicular to a turbulent flow by Vickery (1965). It has also been found to agree well with admittance functions determined for billboards, which are similar objects to the here investigated heliostat, in wind tunnel experiments by Warnitchai et al. (2009) and Li et al. (2018). The comparison of the Vickery admittance function to the measurement results of this study is discussed in more detail later in the text.

To outline the contribution and impact of the  $S_u$  and  $S_v$  wind spectra, the admittance functions have been determined in two ways, i.e. (a) by taking only the longitudinal wind spectrum  $S_u$  into account (Eq. (15) with  $S_v, S_w = 0$ ) and (b) by considering both  $S_u$  and  $S_v$  (Eq. (15) with  $S_w = 0$ ). For this calculation, the derivatives  $\frac{\partial c_{F_x}}{\partial \beta}$  have been determined from the measured  $\bar{c}_{F_x}$ -course over  $\bar{\beta}$  represented by the black curve in Fig. 6(a).

In Fig. 8(a), it appears that the admittance functions, when solely being calculated from the longitudinal wind spectrum  $S_u$ , deviate slightly where in particular those admittances related to larger angles of attack (yellow, orange admittances) are shifted upward. Yet, with regard to the admittance model (Eq. (15)), it is expected that all admittances follow a similar course (as the impact of varying angles of attack is corrected or removed when applying the full admittance model) and it can therefore be assumed that the lateral wind spectrum  $S_v$  also contributes to the fluctuating drag force and must be taken into account. This is plausible when considering that at large angles of attack, the longitudinal wind component is rather parallel to the concentrator, thus induces less load, while the lateral wind component is rather perpendicular and thus induces more load. This can be verified when determining the admittance functions from both  $S_u$  and  $S_v$  as depicted in Fig. 8(b). In this case, the admittance functions are more consistent and follow a similar course which is in accordance with the expectation. Moreover, the admittances as depicted in Fig. 8(b) can be considered close to their final state even though the vertical wind spectrum  $S_w$  has not been taken into account. This is because the derivative  $\frac{\partial c_{F_x}}{\partial \alpha}$  and thus the impact of  $S_w$  can be estimated to be rather small based on results of a wind tunnel study conducted by Peterka et al. (1989) who present a course of  $\bar{c}_{F_x}$  over  $\bar{\alpha}$ . The presented behavior of  $\bar{c}_{F_x}$  over increasing  $\bar{\alpha}$  is similar to the behavior of  $\bar{c}_{F_x}$  over decreasing  $\bar{\beta}$  as depicted in Fig. 6(a). For very large  $\bar{\alpha}$ , the  $\bar{c}_{F_x}$ -values reach their maximum and stay rather constant before they start to decrease between an elevation angle of 70° and 60°. At  $\bar{\alpha} = 60^\circ$ , the slope is still moderate and the term  $(\frac{\partial c_{F_x}}{\partial \alpha})^2$  is about an order of magnitude smaller than the term  $4\bar{c}_{F_x}^2$ . Thus, the impact of  $S_w$  can be

considered negligible and the admittances in Fig. 8(b) are considered to be in their final state.

The derived (mean) aerodynamic admittance function in Fig. 8(b) can be verified by comparing it to the Vickery admittance function shown in gray. It becomes apparent that both admittances agree well as they start to decrease at the same non-dimensional frequency of approximately 0.2 and the slope of the decreasing part is identical up to a non-dimensional frequency of approximately 1. Afterward, the Vickery admittance decreases faster than the measured admittance which is presumably not a physical phenomenon but related to measurement uncertainties of this study. The high frequency range corresponds to small wind speed and load fluctuations which are generally harder to measure through a sensor due to a limited sensitivity. This can be one reason for the measured admittances to deviate from the Vickery admittance towards higher frequencies. Future investigations may study this minor difference further.

Considering the measured mean aerodynamic admittance function in Fig. 8(b), its course over the non-dimensional frequency  $n$  reveals the following aspects. With regard to the explanations in Section 2.2.3, a non-dimensional frequency between 0.1 and 1 indicates that the eddies in the turbulent wind flow are of similar size than the structure, here the heliostat. In fact, the measured admittance function starts to decrease at  $n \approx 0.2$  which suggests that those eddies which are of similar and in particular of smaller size than the heliostat are not fully effective in generating aerodynamic loads, i.e. their effectiveness is reduced. On the other hand, as the aerodynamic admittance tends towards unity for  $n < 0.2$ , those eddies which are just about the size of the heliostat and in particular larger are fully effective in generating loads. These large eddies engulf the entire heliostat and act in a quasi-static manner (i.e. similar to the mean flow).

Lastly, it shall be emphasized that the aerodynamic admittance function only provides information on the *effectiveness* of certain size eddies to generate loads on the heliostat. It does not directly provide information on the *amount* of load. The amount of load is determined by the strength of the wind speed fluctuation associated with a certain size eddy which is represented by the wind spectrum.

### 3.3.2. Admittance function of aerodynamic moment about $y_h$ -axis

The admittance functions of  $M_{y_h}$  are depicted in Figs. 9(a) and 9(b), again separately determined by (a) taking solely the wind spectrum  $S_u$  into account and (b) taking both  $S_u$  and  $S_v$  into account. With regard to the initial explanations, the fluctuating moment  $M_{y_h}$  is expected to be predominantly induced by the lateral wind spectrum  $S_v$  for very small and large angles of attack which can be verified by Figs. 9(a) and 9(b). When taking into account the impact of the longitudinal

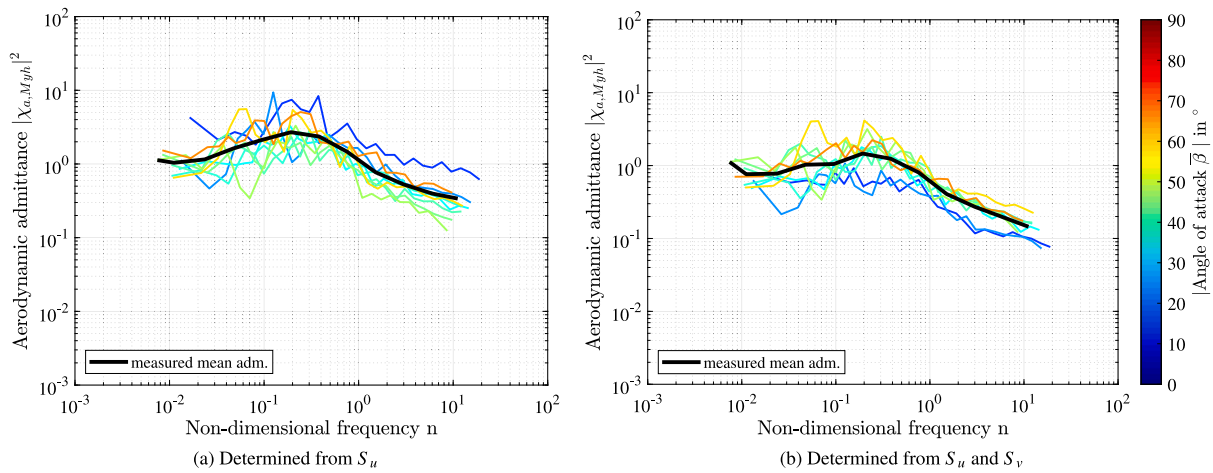


Fig. 9. Aerodynamic admittance functions of the moment  $M_{y_h}$ . Impact of  $S_w$  assumed negligible. Therefore, depicted admittances in (b) are considered in their final state. (For interpretation of the references to color in this figure legend, the reader is referred to the web version of this article.)

wind spectrum  $S_u$  only, the admittance function corresponding to the smallest angle of attack (dark blue curve in Fig. 9(a)) does not match the remaining admittance functions well. In contrast, when taking into account both  $S_u$  and  $S_v$ , the admittances in Fig. 9(b) are more consistent and the mean admittance function follows a course which is close to the expected one, i.e. it tends towards unity for very small frequencies and decreases towards larger frequencies. The mean admittance function in Fig. 9(b) is again considered close to its final state even though the vertical wind spectrum  $S_w$  has not been taken into account. Yet, the derivative  $\frac{\partial c_{M_{yh}}}{\partial \alpha}$  can be estimated to be rather small at an elevation angle of  $60^\circ$  based on the following explanations. Imagining the behavior of the pressure distribution for constant  $\bar{\beta}$  but varying  $\bar{\alpha}$ , it is expected that the position of the RHP significantly moves in vertical direction while in horizontal direction, the position is expected to be rather constant. This behavior is similar to the RHP behavior when  $\bar{\beta}$  varies but  $\bar{\alpha}$  is constant which had been discussed previously to explain the course of  $\bar{c}_{M_{xh}}$ . Therefore, the behavior of  $\bar{c}_{M_{yh}}$  over increasing  $\bar{\alpha}$  can be assumed similar to the behavior of  $\bar{c}_{M_{xh}}$  over decreasing  $\bar{\beta}$ . With regard to Fig. 7(a), the course of  $\bar{c}_{M_{xh}}$  over  $\bar{\beta}$  at  $\bar{\beta} = 30^\circ$  is rather flat which, according to the previous explanations, is assumed to be equivalent to the course of  $\bar{c}_{M_{yh}}$  over  $\bar{\alpha}$  at  $\bar{\alpha} = 60^\circ$ . Hence, the derivative  $\frac{\partial c_{M_{yh}}}{\partial \alpha}$  and thus the impact of  $S_w$  on the fluctuating moment about the  $y_h$ -axis can be considered negligibly small (for an elevation angle of  $\bar{\alpha} = 60^\circ$ ) and the mean admittance function of  $M_{y_h}$  in Fig. 9(b) is assumed close to its final state.

### 3.3.3. Admittance function of aerodynamic moment about $x_h$ -axis

Analogously to the admittances of the moment  $M_{y_h}$ , the admittance functions of the moment  $M_{x_h}$  are presented in Fig. 10. Yet, the following note must be given. Based on the same argumentation as mentioned before, the course of  $\bar{c}_{M_{xh}}$  over increasing  $\bar{\alpha}$  can be estimated to be similar to the course of  $\bar{c}_{M_{yh}}$  over decreasing  $\bar{\beta}$ . Taking the course of  $\bar{c}_{M_{yh}}$  in Fig. 7(b) into account, it appears that the derivative  $\frac{\partial c_{M_{yh}}}{\partial \beta}$  at  $\bar{\beta} = 30^\circ$  is comparably large which indicates that the derivative  $\frac{\partial c_{M_{xh}}}{\partial \alpha}$  at  $\bar{\alpha} = 60^\circ$  must be expected to be rather large. Hence, the impact of the vertical wind spectrum  $S_w$  cannot be assumed negligible when calculating the admittances of the moment  $M_{x_h}$  (for an elevation angle of  $\bar{\alpha} = 60^\circ$ ). Therefore, the admittances in Fig. 10 cannot be considered in their final state. Nevertheless, the following conclusion can be drawn. A comparison of Figs. 10(a) and 10(b) indicates that for larger angles of attack, the lateral spectrum  $S_v$  contributes significantly

to the fluctuating moment  $M_{x_h}$ . This conclusion is drawn because the admittances in Fig. 10(a) related to larger angles of attack (yellow, orange admittances) are notably shifted upward and do not match the remaining admittances well when solely considering the impact of  $S_u$ . On the other hand, when applying the model representation under consideration of both  $S_u$  and  $S_v$ , the admittance functions in Fig. 10(b) are very consistent. Still, the course of the mean admittance function in Fig. 10(b) differs from the admittance course of  $M_{y_h}$  and in particular differs from the expected course. Presumably, this is due to the non-negligible impact of the vertical wind spectrum  $S_w$  which could not be considered in this evaluation. A further explanation for the deviation of the mean admittance function from the expected course could be vortex shedding. The course of the mean admittance function in Fig. 10(b) exhibits a widely stretched peak which can imply that a moment about the  $x_h$ -axis was induced by vortices that regularly shed from the top and bottom of the concentrator. Such shedding frequency is typically described through the non-dimensional Strouhal number which was found to be approximately 0.18 for a heliostat at  $\bar{\alpha} = 60^\circ$  by Mammar et al. (2018). The definition of the Strouhal number is identical to the non-dimensional frequency  $n$  depicted in Fig. 10(b) and it becomes apparent that the widely stretched peak is in the range of  $n = 0.18$ , thus the potential occurrence of vortex shedding is plausible. Nevertheless, it shall be noted again that the depicted admittances in Fig. 10(b) are not in their final state because the vertical wind spectrum  $S_w$  could not be taken into account during evaluation due to the non-evaluable derivative  $\frac{\partial c_{M_{xh}}}{\partial \alpha}$ . At the same time, such derivative was concluded to be non-negligible in case of the  $M_{x_h}$ -admittances (for an elevation angle of  $\bar{\alpha} = 60^\circ$ ) so a further evaluation is necessary in future, including the impact of  $S_w$ , to verify the occurrence of vortex shedding. Lastly, note that the impact of vortex shedding can vary for different elevation angles which must also be further investigated in future as the scope of this study was limited to only one elevation angle ( $\bar{\alpha} = 60^\circ$ ).

## 4. Summary and conclusion

Full-scale experimental investigations of the wind-induced loads on heliostats are important to complement small-scale wind tunnel and numerical studies. Therefore, in this study a field measurement campaign was conducted for a  $48.5 \text{ m}^2$  pentagonal Stellio heliostat which was installed at the DLR site in Juelich. In total, nine individual 10-minute measurement periods were conducted during which the approaching wind was measured through ultrasonic anemometers. Simultaneously, the pressure distribution over the Stellio concentrator was measured



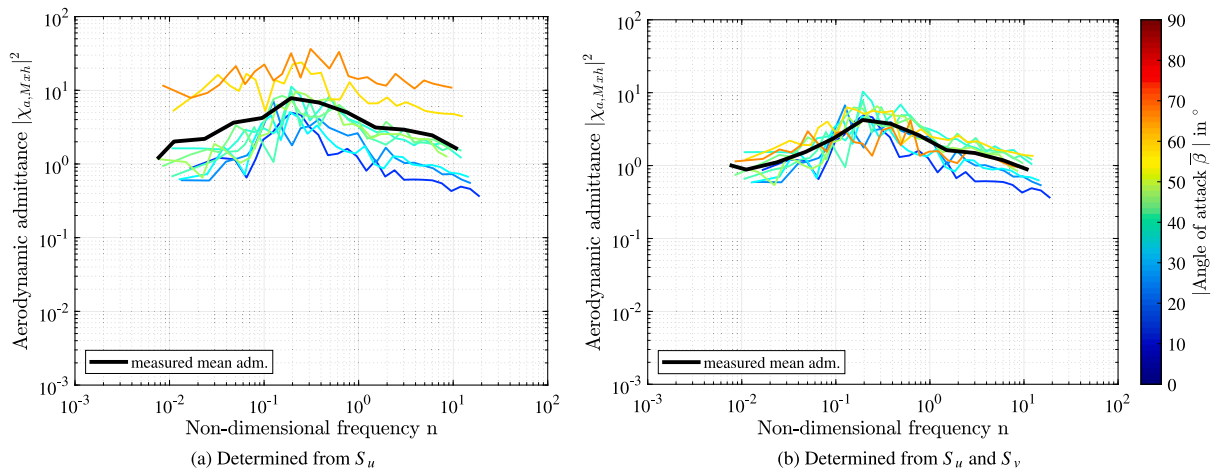


**Fig. 10.** Aerodynamic admittance functions of the moment  $M_{x_p}$ . Impact of  $S_w$  expected to be non-negligible. Therefore, depicted admittances are not in their final state. (For interpretation of the references to color in this figure legend, the reader is referred to the web version of this article.)

through a newly developed pressure measurement system. During the nine measurement periods, the mean vertical angle of attack, determined by the elevation angle, was fixed to  $\bar{\alpha} = 60^\circ$  while the mean horizontal angle of attack  $\bar{\beta}$  varied. Based on the wind and pressure measurements of the nine periods, the non-dimensional pressure distributions, the load coefficients and the aerodynamic admittance functions were studied and gave an insight into the aerodynamics of a real-scale heliostat. The non-dimensional mean pressure distributions showed very consistent  $\bar{c}_p$ -values between 2.2 and 2.6 within the region of highest pressure coefficients. These values agreed well with results of a wind tunnel study conducted by [Emes et al. \(2019\)](#). Moreover, the pressure distributions showed that with increasing angles of attack  $\bar{\beta}$ , the region of highest pressure coefficients moves from the center of the concentrator towards the edge, i.e. in horizontal concentrator direction, while it does not significantly move in vertical concentrator direction due to a fixed elevation angle. Based on this behavior of the pressure distribution, the mean drag and lift force coefficients,  $\bar{c}_{F_x}$  and  $\bar{c}_{F_z}$ , as well as the mean moment coefficients about the horizontal concentrator axis  $\bar{c}_{M_{x_h}}$  were found to reach maximum values at very small angles of attack while they decreased significantly towards larger angles of attack. In contrast, the mean moment coefficients about the vertical concentrator axis  $\bar{c}_{M_{y_h}}$  reached minimum values for very small and large angles of attack while their maximum was found to be at an angle of attack of approximately  $50^\circ$ . Lastly, the aerodynamic admittances  $|\chi_a|^2$  of the different load components were evaluated and it was found that they start to decrease at a non-dimensional frequency of approximately 0.2. This finding indicates that eddies which are about the size of the heliostat or larger are fully effective in generating aerodynamic loads while the effectiveness of smaller eddies is reduced.

In conclusion, this study provided a first valuable insight into the aerodynamics of a real-scale heliostat. While the scope of this study was limited to nine measurement periods, the presented experimental method is easy-to-apply and can be used for comprehensive field studies in the future. Based on a larger data basis, a detailed comparison to wind tunnel results can for example be performed. By that, optimization potential for heliostat designs may be explored in future as heliostats are often designed based on the results of wind tunnel studies. Moreover, as the investigated moments about the concentrator axes are the cause of wind-induced tracking deviations, the here conducted field study as well as future field studies can contribute to a better understanding and prediction of wind-induced optical errors of heliostats.

## Declaration of competing interest

The authors declare that they have no known competing financial interests or personal relationships that could have appeared to influence the work reported in this paper.

## Acknowledgments

The authors gratefully acknowledge the financial support of the German Federal Ministry for Economic Affairs and Climate Action (Heliodor contract 0324310 and AdaptedHelio contract 03EE5056). The authors would furthermore like to thank Wolfgang Zinburg and Martin Blume for their tremendous and indispensable contribution to the development of the pressure measurement system, as well as Tim Kindler for his great contribution to the post processing and evaluation of the pressure data. The authors would finally like to thank sbp sonne GmbH for providing and operating the Stellio heliostat, as well as the anonymous reviewers for their valuable comments to the manuscript.

## References

- Balz, M., Göcke, V., Keck, T., von Reeken, F., Weinrebe, G., Wöhrbach, M., 2016. Stellio – development, construction and testing of a smart heliostat. AIP Conf. Proc. 1734, 020002. <http://dx.doi.org/10.1063/1.4949026>.
- Banks, D., 2011. Measuring peak wind loads on solar power assemblies. In: The 13th. International Conference on Wind Engineering. Amsterdam, Netherlands.
- Blume, K., Röger, M., Pitz-Paal, R., 2023. Simplified analytical model to describe wind loads and wind-induced tracking deviations of heliostats. Revised manuscript under review.
- Blume, K., Röger, M., Schlichting, T., Macke, A., Pitz-Paal, R., 2020. Dynamic photogrammetry applied to a real scale heliostat: Insights into the wind-induced behavior and effects on the optical performance. Sol. Energy 212, 297–308. <http://dx.doi.org/10.1016/j.solener.2020.10.056>.
- Dyrbye, C., Hansen, S.O., 1999. Wind Loads on Structures. Wiley, Chichester, England.
- Emes, M.J., Arjomandi, M., Ghanadi, F., Kelso, R.M., 2017. Effect of turbulence characteristics in the atmospheric surface layer on the peak wind loads on heliostats in stow position. Sol. Energy 157, 284–297. <http://dx.doi.org/10.1016/j.solener.2017.08.031>.
- Emes, M.J., Jafari, A., Ghanadi, F., Arjomandi, M., 2019. Hinge and overturning moments due to unsteady heliostat pressure distributions in a turbulent atmospheric boundary layer. Sol. Energy 193, 604–617. <http://dx.doi.org/10.1016/j.solener.2019.09.097>.
- Emes, M.J., Jafari, A., Pfahl, A., Coventry, J., Arjomandi, M., 2021. A review of static and dynamic heliostat wind loads. Sol. Energy 225, 60–82. <http://dx.doi.org/10.1016/j.solener.2021.07.014>.
- Holmes, J.D., 2015. Wind Loading of Structures. vol. 3, CRC Press, Boca Raton, USA, <http://dx.doi.org/10.1201/b18029>.
- Hucho, W.-H., 2011. Aerodynamik der stumpfen Körper. Vol. 2, Vieweg + Teubner Verlag, Wiesbaden, <http://dx.doi.org/10.1007/978-3-8348-8243-1>.

- Jafari, A., Ghanadi, F., Arjomandi, M., Emes, M.J., Cazzolato, B.S., 2019. Correlating turbulence intensity and length scale with the unsteady lift force on flat plates in an atmospheric boundary layer flow. *J. Wind Eng. Ind. Aerodyn.* 189, 218–230. <http://dx.doi.org/10.1016/j.jweia.2019.03.029>.
- Kwok, K.C.S., 2013. Wind-induced vibrations of structures: With special reference to tall building aerodynamics. In: Tamura, Y., Kareem, A. (Eds.), *Advanced Structural Wind Engineering*. pp. 121–155. [http://dx.doi.org/10.1007/978-4-431-54337-4\\_5](http://dx.doi.org/10.1007/978-4-431-54337-4_5).
- Li, Z., Wang, D., Chen, X., Liang, S., Li, J., 2018. Wind load effect of single-column-supported two-plate billboard structures. *J. Wind Eng. Ind. Aerodyn.* 179, 70–79. <http://dx.doi.org/10.1016/j.jweia.2018.05.013>.
- Mammar, M., Djouimaa, S., Gärtner, U., Hamidat, A., 2018. Wind loads on heliostats of various column heights: An experimental study. *Energy* 143, 867–880. <http://dx.doi.org/10.1016/j.energy.2017.11.032>.
- Nieffer, D., Effertz, T., Macke, A., Röger, M., Weinrebe, G., Ulmer, S., 2019. Heliostat testing according to SolarPACES task III guideline. *AIP Conf. Proc.* 2126, 030039. <http://dx.doi.org/10.1063/1.5117551>.
- Peterka, J.A., Tan, Z., Cermak, J.E., Bienkiewicz, B., 1989. Mean and peak wind loads on heliostats. *J. Solar Energy Eng.* 111, 158–164. <http://dx.doi.org/10.1115/1.3268302>.
- Petersen, C., Werkle, H., 2017. *Dynamik der Baukonstruktionen*. Vol. 2, Springer Vieweg, Wiesbaden, <http://dx.doi.org/10.1007/978-3-8348-2109-6>.
- Pfahl, A., 2018. *Wind Loads on Heliostats and Photovoltaic Trackers (Dissertation)*. Technische Universiteit Eindhoven, Eindhoven, Netherlands.
- Pfahl, A., Buselmeier, M., Zschke, M., 2011a. Determination of wind loads on heliostats. In: *Proceedings of the 17th SolarPACES Conference*. Granada, Spain.
- Pfahl, A., Buselmeier, M., Zschke, M., 2011b. Wind loads on heliostats and photovoltaic trackers of various aspect ratios. *Sol. Energy* 85, 2185–2201. <http://dx.doi.org/10.1016/j.solener.2011.06.006>.
- Pfahl, A., Randt, M., Meier, F., Zschke, M., Geurts, C.P.W., Buselmeier, M., 2015. A holistic approach for low cost heliostat fields. *Energy Procedia* 69, 178–187. <http://dx.doi.org/10.1016/j.egypro.2015.03.021>.
- Ruscheweyh, H., 1982. *Dynamische Windwirkung an Bauwerken - Band 2: Praktische Anwendungen*. Bauverlag, Wiesbaden, Berlin.
- Sensirion, A., 2017. Application note for sensirion differential pressure sensors (SDP): Mass flow temperature compensation & sensor selection guide. Report, Sensirion AG, Staefa, Switzerland, URL [https://sensirion.com/media/documents/DFC65EB3/6166C638/Sensirion\\_Differential\\_Pressure\\_AppNotes\\_Selection\\_Guide\\_V3.1\\_1.pdf](https://sensirion.com/media/documents/DFC65EB3/6166C638/Sensirion_Differential_Pressure_AppNotes_Selection_Guide_V3.1_1.pdf).
- Stull, R.B., 1988. *An Introduction to Boundary Layer Meteorology*. Kluwer Academic, Dordrecht, Netherlands.
- Vickery, B.J., 1965. On the flow behind a coarse grid and its use as a model of atmospheric turbulence in studies related to wind loads on buildings. Report, National Physical Laboratory, Great Britain.
- Warnitchai, P., Sinthuwong, S., Poemsantitham, K., 2009. Wind tunnel model tests of large billboards. *Adv. Struct. Eng.* 12 (1), 103–114. <http://dx.doi.org/10.1260/136943309787522650>.
- Wu, Z., Gong, B., Wang, Z., Li, Z., Zang, C., 2010. An experimental and numerical study of the gap effect on wind load on heliostat. *Renew. Energy* 35, 797–806. <http://dx.doi.org/10.1016/j.renene.2009.09.009>.
- Yu, J.S., Emes, M.J., Ghanadi, F., Arjomandi, M., Kelso, R., 2019. Experimental investigation of peak wind loads on tandem operating heliostats within an atmospheric boundary layer. *Sol. Energy* 183, 248–259. <http://dx.doi.org/10.1016/j.solener.2019.03.002>.